第39卷第3期
2023年3月

无 机 化 学 学 报
CHINESE JOURNAL OF INORGANIC CHEMISTRY

Vol.39 No.3
533-544

可见近红外光响应直接Z型异质结光催化剂 $LaNiO_3$/CdS的产氢性能

王兆宇[1,2] 杨兆杰[1] 程锦添[1] 陈锦溢[1] 张明文*[,1,2]

([1]福建技术师范学院,近海流域环境测控治理福建省高校重点实验室,福清 350300)

([2]福州大学化学学院,能源与环境光催化国家重点实验室,福州 350002)

摘要: 通过冷凝-回流方式制备可见近红外光响应直接Z型 $LaNiO_3$/CdS纳米复合物,在对其进行物理化学表征后将其应用于光解水产氢反应。在可见光照射下,$LaNiO_3$/CdS光催化剂在5 h的 H_2 产量达到737 μmol,其 H_2 产量是CdS的4.3倍(172 μmol)。光电化学测试证实,$LaNiO_3$/CdS之间异质结的构筑能有效地促进光生载流子在界面的迁移、分离,从而促进其光解水产氢效率和稳定性的提高。同时随着近红外光的引入,其产氢活性提高至996 μmol。在上转换荧光测试中,$LaNiO_3$ 在808 nm光激发下在406和628 nm显示出发射荧光,这表明其能在近红外光照射下产生光生载流子,从而进一步提高其光解水产氢效率。

关键词: $LaNiO_3$/CdS纳米杂化物; 光解水产氢反应; 近红外光响应; 异质结; 上转换荧光

中图分类号: O643.3 **文献标识码:** A **文章编号:** 1001-4861(2023)03-0533-12

DOI: 10.11862/CJIC.2023.007

Vis-NIR light-responsive direct Z-scheme $LaNiO_3$/CdS heterojunction photocatalysts for H_2 evolution

WANG Zhao-Yu[1,2] YANG Zhao-Jie[1] CHENG Jin-Tian[1] CHEN Jin-Yi[1] ZHANG Ming-Wen*[,1,2]

([1]*Fujian Provincial Key Lab of Coastal Basin Environment, Fujian Polytechnic Normal University, Fuqing, Fujian* 350300, *China*)

([2]*State Key Laboratory of Photocatalysis on Energy and Environment, College of Chemistry, Fuzhou University, Fuzhou* 350002, *China*)

Abstract: The Vis-NIR light-responsive direct Z-scheme $LaNiO_3$/CdS nanohybrid was synthesized via a refluxing method, fully characterized, and used in photocatalytic H_2 evolution. The H_2 evolved over $LaNiO_3$/CdS photocatalyst in 5 h was 737 μmol under visible light irradiation, which was 4.3 times that over CdS (172 μmol) ascribed to the formed heterojunction between $LaNiO_3$ and CdS. Moreover, the introduced $LaNiO_3$ extended the light absorption to the NIR region and the H_2 evolution increased to 996 μmol under Vis-NIR light irradiation. $LaNiO_3$ exhibited upconversion luminescence at 406 and 628 nm when excited at 808 nm, which means that $LaNiO_3$ can generate charge carriers under NIR light irradiation, thereby further improving the efficiency of its photocatalytic H_2 evolution.

Keywords: $LaNiO_3$/CdS nanohybrid; photocatalytic H_2 evolution; NIR light-responsive; heterojunction; upconversion luminescence

Artificial photosynthesis based on semiconductors is considered to be a hopeful technology to solve the worldwide energy crisis and environmental pollution[1-4]. However, a problem is that only ultraviolet (UV) light, which accounts for 5% of the total solar energy, can be harvested by some commonly used semi-

收稿日期:2022-08-16。收修改稿日期:2022-12-04。

国家自然科学基金(No.21902026)、福建省自然科学基金(No.2020J05244,2020J05241,2020J01303,2022J01983)、福建省中青年教师教育科研项目(No.JAT210377)资助。

*通信联系人。E-mail:mwzhang1989@163.com

conductors, such as TiO_2, ZnO, and SnO_2. Compared with UV light, visible and NIR light has a strong penetrating capacity, which is of benefit for sufficient contact with substrates and solid-liquid photocatalytic process[5-7]. Furthermore, the photocatalytic activity over most photocatalysts is only moderate due to the high recombination rate of photo-generated carriers in the semiconductor[8-9]. Therefore, it must be of significance to explore high-efficiency photocatalysts with Vis-NIR response.

Ternary metal oxide has been intensively investigated in the fields of fuel cells, DRM catalysis, and photocatalysis owing to their unique structures and high stability[10-12]. However, there exist much fewer reports on the use of ternary metal oxide material as active photocatalysts for improving H_2 evolution under Vis-NIR light irradiation. Qin fabricated $ZnO/ZnFe_2O_4$ nanocomposite for organic dye degradation, which exhibits excellent photocatalytic performance due to the formation of heterojunction and the enhanced light absorption in the Vis-NIR region with the introduction of $ZnFe_2O_4$[13]. Ding demonstrated that $CdS/NiTiO_3$ show superior photocatalytic activity for H_2 evolution in the Vis-NIR region because the $NiTiO_3$ show NIR light response which will contribute to H_2 evolution[14]. The above research implies that the ternary metal oxide exhibits NIR light absorption which will contribute to photocatalysis, thus the ternary metal oxide may be an effective candidate for the development of wide-spectrum responsive photocatalysts[15-16]. Ternary metal oxide lanthanum nickelate ($LaNiO_3$) has been demonstrated as an active photocatalyst for H_2 evolution. In the crystal structure of $LaNiO_3$, the La cation is 12-fold coordinated and the Ni cation is 6-fold coordinated to the oxygen anions. The strong hybridization between the O2*p* and the transition-metal 3*d* orbitals in the $[NiO_6]$ octahedra could induce structural distortions and/or Ni site valence transformations, thus modifying the physicochemical properties for enhanced performance[17-19]. $LaNiO_3$ has a narrow band gap of 1.9 eV which can be excited by visible light. Moreover, $LaNiO_3$ shows intense light absorption during the Vis-NIR region and exhibits upconversion luminescence under NIR light irradiation which may endow $LaNiO_3$ with photocatalysis activity under Vis-NIR light irradiation. Metal sulfides have been extensively studied for photocatalytic H_2 under visible light irradiation due to their narrower band gaps and lower conduction band (CB) positions. Among various metal sulfides, CdS exhibit photocatalytic activity for H_2 evolution in the presence of a sacrificial agent under visible light irradiation[20-22]. Unfortunately, the pure CdS still show lower activity and serious photocorrosion caused by the high recombination rate of the photoinduced electron-hole pairs. There are several methods to overcome its drawbacks, and the construction of direct Z-scheme heterojunction is an effective approach to both improve photocatalytic activity and inhibit photocorrosion[23-24].

Compared with the common type-Ⅱ heterojunction, the direct Z-scheme heterojunction is more favorable which can not only accelerate the spatial separation efficiency of photoinduced electron-hole pairs but also maximize the higher reduction and oxidation potentials in hybrid photocatalysts. In the direct Z-scheme heterojunction system, the photoinduced electrons on the CB of component A will recombine with the holes on the valence band (VB) of component B (Fig. 1). Consequently, the photoinduced electrons and holes accumulated on the CB of component B and the VB of component A can be used for reduction and oxidation reaction, respectively. Hence, the direct Z-

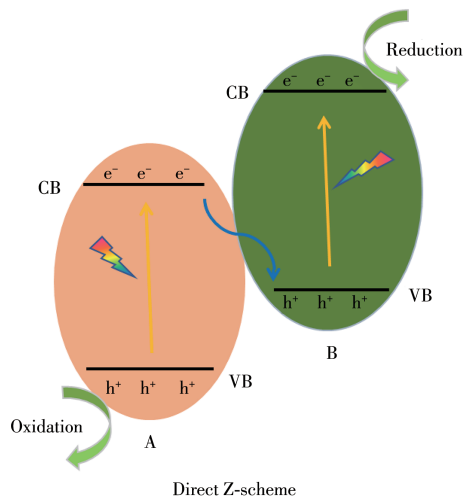

Fig.1 Schematic of the charge transfer in a direct Z-scheme photocatalytic system

scheme photocatalytic heterojunction achieves high redox potential and effective spatial separation of photoinduced electron-hole pairs, contributing to photocatalytic reaction. The construction of direct Z-scheme heterojunction between CdS and suitable semiconductors has indeed been verified to be an effective way to achieve superior photocatalytic performance[25-26]. The CB position of $LaNiO_3$ (0.21 V) is higher than the VB position of CdS, and thus photo-generated electrons in the CB of $LaNiO_3$ can recombine with the photo-generated holes in the VB of CdS in $LaNiO_3$/CdS composites, which makes it possible to construct the direct Z-scheme heterojunction. Thus, it can be anticipated that the hybridization of CdS with $LaNiO_3$ may form a direct Z-scheme heterojunction photocatalyst for solar energy conversion under Vis-NIR light irradiation.

Herein, a novel direct Z-scheme $LaNiO_3$/CdS nanohybrid with a wide spectrum response was fabricated via a refluxing method and employed as a novel photocatalyst for H_2 evolution under Vis-NIR light illumination. The $LaNiO_3$/CdS nanohybrid exhibited improved photocatalytic performance for photocatalytic performance due to the construction of direct Z-scheme heterojunction between $LaNiO_3$ and CdS, which was demonstrated by photoelectrochemical (PEC) tests. Moreover, $LaNiO_3$ exhibited luminescence at 406 and 628 nm when excited at 808 nm, which means that $LaNiO_3$ can generate electrons and holes under irradiation of NIR light for H_2 evolution.

1 Experimental

All reagents were supplied by Aladdin Chemical Reagent Factory (Shanghai, China) and used without further purification. Deionized (DI) water was used in this work.

1.1 Synthesis of $LaNiO_3$/CdS

The $LaNiO_3$ nanoparticles were synthesized according to the reported literature[27]. The $LaNiO_3$/CdS nanohybrid was synthesized from as-prepared $LaNiO_3$ nanoparticles, $Cd(OAc)_2$, and thiourea via a refluxing method, as shown in Fig.2. $Cd(OAc)_2$ (0.2 mol·L^{-1}, 10 mL) were added to a suspension containing $LaNiO_3$ in DMF (70 ml) under continuous stirring. After that, a solution of thiourea in DMF (1.0 mol·L^{-1}, 6 mL) was added to the above suspension and the resultant suspension was refluxed at 160 ℃ for 6 h. The obtained product was filtrated, washed with ethanol, and dried at 60 ℃ in a vacuum overnight. The harvested samples were denoted as w%-$LaNiO_3$/CdS, where w (w=0, 10, 20, 30, 40, 50, 100) is the theoretical mass fraction value of $LaNiO_3$ in the $LaNiO_3$/CdS nanohybrid. For comparison, CdS were synthesized in a similar method. The used w%-$LaNiO_3$/CdS nanohybrid for characterization and photocatalytic evaluation is the 30%-$LaNiO_3$/CdS nanohybrid unless otherwise stated.

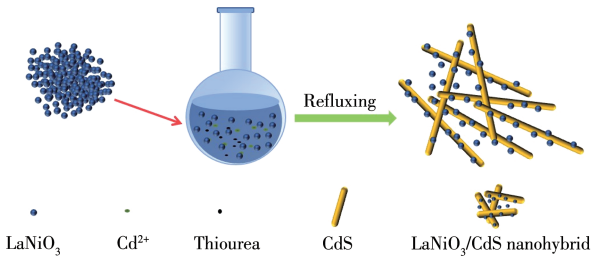

Fig.2 Schematic preparation process for the $LaNiO_3$/CdS nanohybrid

1.2 Characterization

The powder X-ray diffraction (XRD) patterns of the samples were obtained using a Bruker D8 Advance instrument (Cu $K\alpha$ irradiation, λ=0.154 06 nm, U=40 kV, I=40 mA, 2θ=20°-80°). Transmission electron microscope (TEM) images were obtained on a transmission electron microscope (JEM-2100F, JEOL, Japan) with an accelerating voltage of 200 kV. The scanning electron microscope (SEM) images and Energy-dispersion X-ray analysis (EDX) spectra were captured using a Hitachi New Generation SU8010 field emission scanning electron microscope with an accelerating voltage of 15 kV. The nitrogen (N_2) adsorption-desorption isotherms of the $LaNiO_3$/CdS nanohybrid were obtained by using an ASAP 2020M apparatus (Micromeritics Instrument Co., USA) at 77 K. The X-ray photoelectron spectroscopy (XPS) spectra were acquired on a PHI Quantum 2000 XPS system equipped with a monochromatic Al $K\alpha$ source and a charge neutralizer. Photoluminescence (PL) characterizations were conducted on an Edinburgh FL/FS900 spectrophotometer at room temperature. The fluorescence lifetime was measured by

recording the time-resolved fluorescence emission spectra in a Deltapro Fluorescence Lifetime System. The upconversion spectrum was measured on a Hitachi F-7000 spectrometer equipped with a commercial 808 nm NIR laser. PEC characterization was performed on a ZENNIUM electrochemical workstation (Zahner, Germany), using a three electrodes cell with a Pt electrode and Ag/AgCl electrode as the counter electrode and reference electrode, respectively. Typically, the catalyst (5 mg) was dispersed in DMF (1 mL). Then, the mixture was spread on the FTO (fluorine-doped tin oxide) glass with an area of *ca*. 0.25 cm^2 and dried at room temperature. The detailed microstructures were observed on transmission electron microscopy (TEM, JEOL model JEM 2010 EX).

1.3 Photocatalytic H_2 evolution

The photocatalytic H_2 evolution activity was performed in a 250 mL Pyrex reaction cell connected to a closed gas-circulation system. In a typical experiment, 20 mg of the catalyst powder was dispersed in 100 mL of an aqueous solution containing Na_2S and Na_2SO_3 as sacrificial reagents. Before the irradiation, the system was vacuumed for 30 min to remove the air. A Xe lamp (300 W) with a long-pass UV cut-off filter (λ>420 nm) was used as the light source. The reaction temperature was controlled at 5 ℃ by cooling water during the reaction process. The produced H_2 was analyzed using a gas chromatograph (Agilent 7820A) equipped with a TDX-01 packed column and a thermal conductivity detector (TCD).

2 Results and discussion

2.1 Morphologies and structural characterization

The crystalline phase of the samples was investigated by XRD. The XRD pattern of as-prepared $LaNiO_3$/CdS confirms the coexistence of CdS and $LaNiO_3$ (Fig. 3). In addition to peaks at 24.9°, 26.7°, 28.5°, 36.9°, 44.1°, 48.1°, and 52.2°, which can be ascribed to the (100), (002), (101), (102), (110), (103), and (112) plane of the hexagonal CdS phase (PDF No. 01-080-0006) [28-29], the XRD pattern of the as-prepared sample also shows diffraction peaks at 32.5°, 48.2°, and 58.6°, corresponding to the (110), (202), and (122) planes of orthorhombic $LaNiO_3$ (PDF No.00-033-0711) [30]. The results of powder XRD measurements demonstrate the successful formation of the $LaNiO_3$/CdS hybrid material.

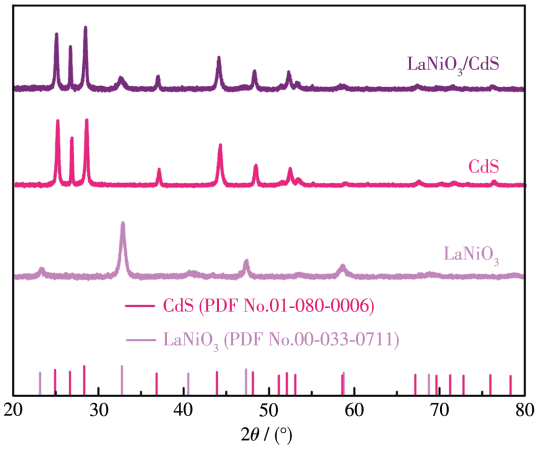

Fig.3 XRD patterns of $LaNiO_3$, CdS, and the $LaNiO_3$/CdS nanohybrid

The morphologies and structures of the as-prepared samples were investigated by SEM and TEM. As shown in Fig.4a, CdS presented a nanorod structure of 50 nm in diameter and 1 μm in length. Pure $LaNiO_3$ displayed irregular and aggregated blocks composed of agglomerated nanoparticles (Fig. 4b). For the $LaNiO_3$/CdS nanohybrid, $LaNiO_3$ was divided into nanoparticles and mixed with CdS nanorods (Fig.4c). The high-resolution TEM (HRTEM) image showed lattice fringes of 0.316 and 0.384 nm, which can be assigned to the (101) and (101) planes of CdS and $LaNiO_3$, respectively (Fig.4d). The clear interface of the $LaNiO_3$/CdS nanohybrid indicates the formation of heterojunction between $LaNiO_3$ and CdS component, promoting the migration of photoinduced electron-hole pairs and separation efficiency over the composites, contributing to the photocatalytic reaction. The presence of La, Ni, O, Cd, and S elements in the $LaNiO_3$/CdS nanohybrid is confirmed by energy-dispersive spectroscopy (EDS) spectra (Fig. S1, Supporting information). The ratio of $LaNiO_3$ and CdS was determined to be 1∶2.1 based on the EDX results, which was comparable to the molar ratio in the starting material.

XPS analyses were conducted to determine the surface chemical composition and electronic state of

the $LaNiO_3$/CdS nanohybrid. In the La3*d* core level spectra of the $LaNiO_3$/CdS nanohybrid (Fig. 5a), the splitting of the main peaks of La3$d_{5/2}$ and La3$d_{3/2}$ were at around 835.9 and 853.1 eV, respectively, and the shake-up satellite peaks of La3$d_{5/2}$ and La3$d_{3/2}$ were at 838.7 and 856.6 eV[31]. As compared with pure $LaNiO_3$ (Fig.5c, 835.6 and 852.6 eV, 838.2 and 855.5 eV), the binding energy of the La3*d* in the $LaNiO_3$/CdS nanohybrid shifted to a higher value by 0.4 eV, indicating an intimate interaction exists between CdS and $LaNiO_3$ component[32-33]. In the meantime, the binding energy of Cd3*d* shifted to a lower value by 0.4 eV as compared with those of CdS (Fig. 5d, 411.6 and 404.8 eV), with Cd3$d_{5/2}$ and Cd3$d_{3/2}$ at 411.2 and 404.4 eV, respectively (Fig. 5b)[34]. The variation of binding energy implied that the electron transfer from $LaNiO_3$ to CdS. No obvious shift of the binding energy was observed for Ni, O, and S (Fig.S2a-S2c and Fig.S3a-S3c).

The specific surface area and pore characteristics of the $LaNiO_3$/CdS nanohybrid were studied by N_2 physisorption measurements. Fig. 6 shows the obtained N_2 adsorption-desorption isotherms, which shape is categorized as the type Ⅳ isotherm with an H1 hysteresis loop. These findings indicate the presence of mesopores in the $LaNiO_3$/CdS nanohybrid. The BET (Brunauer-Emmett-Teller) specific surface area of $LaNiO_3$, CdS, and the $LaNiO_3$/CdS nanohybrid were calculated to be approximately 14, 16, and 20 $m^2 \cdot g^{-1}$, indicating the introduction of $LaNiO_3$ almost do not influence its surface areas. Furthermore, the existence of mesopores in the $LaNiO_3$/CdS nanohybrid will contribute to the mass transport for heterogeneous photoredox reactions.

All the above characterization details indicate the formation of the $LaNiO_3$/CdS nanohybrid. Fig. 7 shows the optical absorption spectra for the obtained samples in a range of 200-1 600 nm. UV-Vis diffuse reflectance (DRS) spectra of the $LaNiO_3$/CdS nanohybrid showed a coupling of the light absorption of both CdS and $LaNiO_3$ by exhibiting an enhanced absorption in the

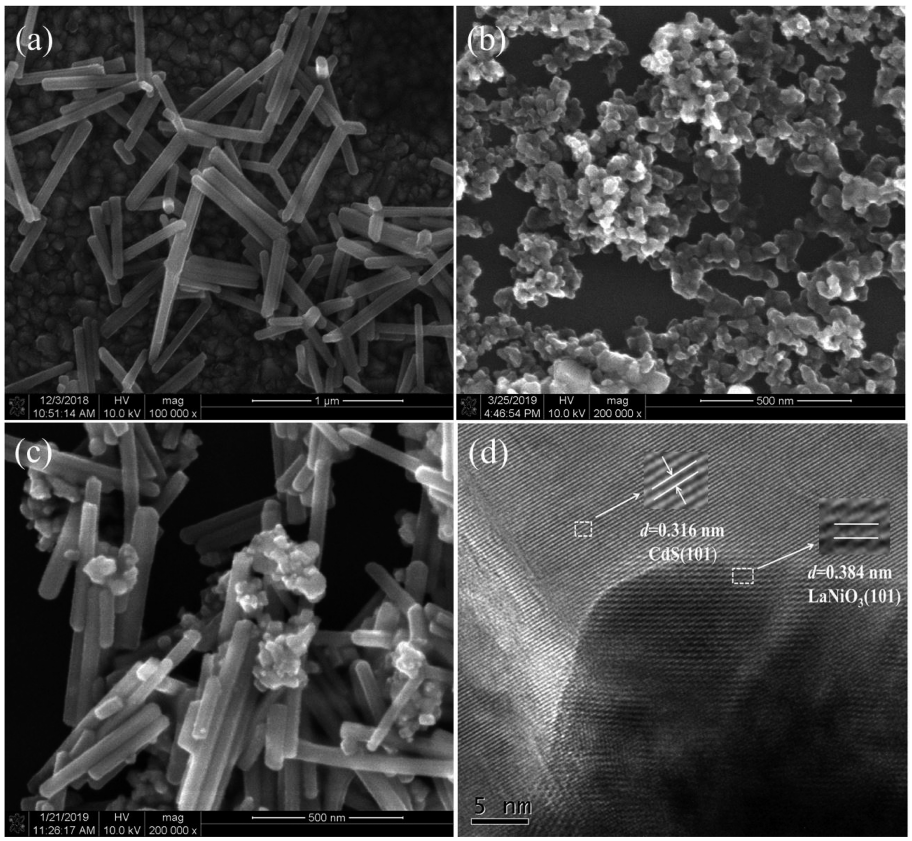

Fig.4 SEM images of CdS nanorods (a), $LaNiO_3$ (b), and the $LaNiO_3$/CdS nanohybrid (c); HRTEM images of the $LaNiO_3$/CdS nanohybrid (d)

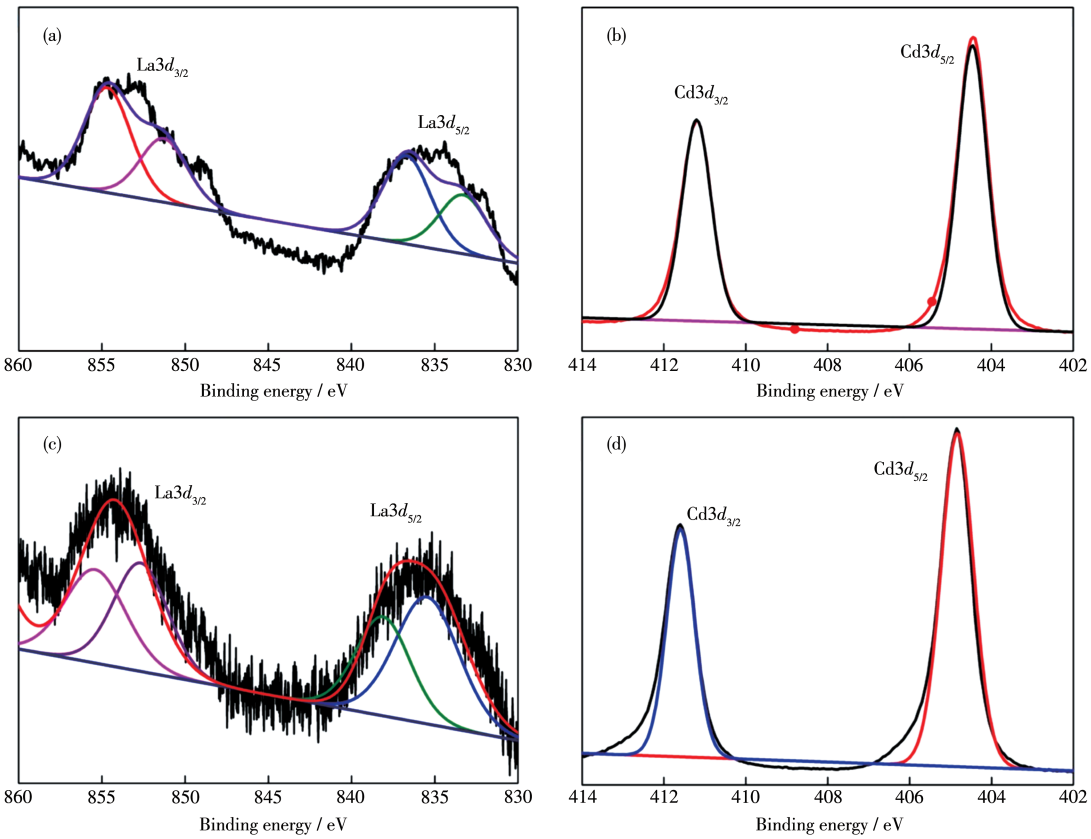

Fig.5 XPS spectra of La3*d* (a) and Cd3*d* (b) for the $LaNiO_3$/CdS nanohybrid; XPS spectra of La3*d* (c) for $LaNiO_3$; XPS spectra of Cd3*d* (d) for CdS

visible light region. Moreover, the $LaNiO_3$/CdS nanohybrid exhibited intense light absorption in the NIR region due to the introduction of $LaNiO_3$, which may endow the $LaNiO_3$/CdS nanohybrid with photocatalytic activity under NIR light irradiation. The background noise at about 800 nm was caused by the variation of the detector.

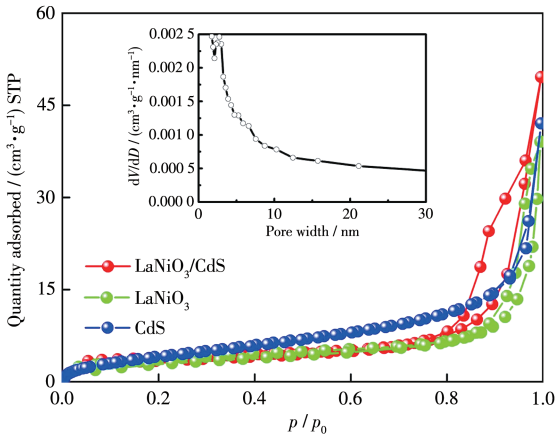

Fig.6 N_2 sorption isotherms of $LaNiO_3$, CdS, and the $LaNiO_3$/CdS nanohybrid

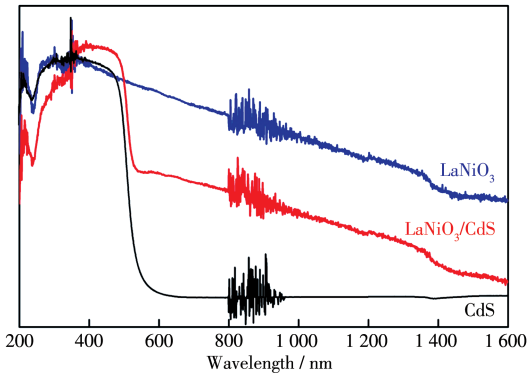

Fig.7 UV-Vis DRS spectra of $LaNiO_3$, CdS, and the $LaNiO_3$/CdS nanohybrid

2.2 Photocatalytic performances and mechanism discussion

The photocatalytic H_2 evolution experiments were performed over the as-prepared catalysts with Na_2S-Na_2SO_3 as a sacrificial agent under visible light irradiation. The CdS was coupled with $LaNiO_3$ to enhance the photocatalytic H_2 evolution furtherly (Fig. 8a). No H_2 was produced over $LaNiO_3$, demonstrating that $LaNiO_3$

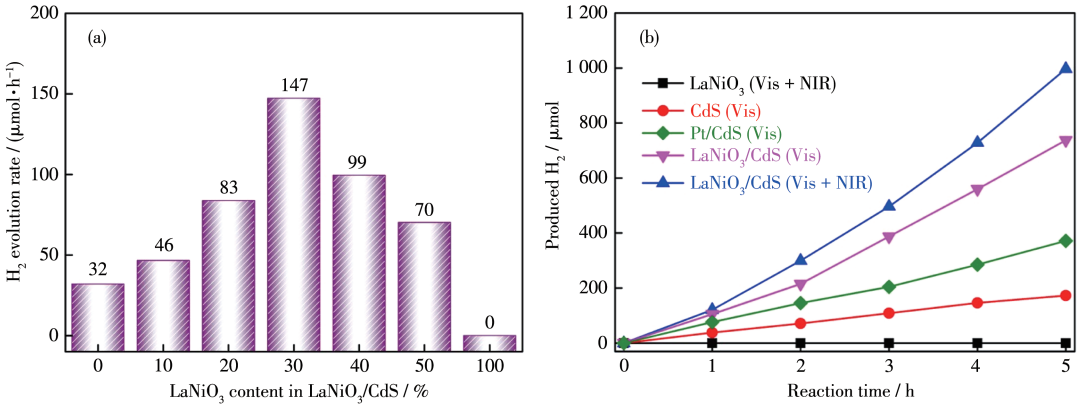

Fig.8 Photocatalytic H_2 evolution over a series of w%-$LaNiO_3$/CdS nanohybrid with different $LaNiO_3$ contents (a); Time-dependent H_2 evolution over $LaNiO_3$, CdS, Pt/CdS, and the $LaNiO_3$/CdS nanohybrid under visible light and Vis-NIR irradiation (b)

alone is not active for photocatalytic H_2 evolution, which may be caused by the lower CB position of $LaNiO_3$ for H_2 evolution and the sluggish migration/separation kinetics of photoinduced electrons and holes. With the addition of $LaNiO_3$ into CdS, the H_2 evolution rate was increased from 32 to 46 μmol·h^{-1} over the $LaNiO_3$/CdS nanohybrid (10% - $LaNiO_3$/CdS). When the $LaNiO_3$ content increased to 30%, 30% - $LaNiO_3$/CdS showed the optimal photocatalytic performance with an H_2 evolution rate of 147 μmol·h^{-1}. Such a noble metal-free H_2 evolution rate was much higher compared with those of other CdS-based photocatalysts in the literature (Table S1). However, with $LaNiO_3$ content in the hybrid increased to 40% (40% - $LaNiO_3$/CdS), a decrease in H_2 production was observed, which may be caused by the light shielding effect of excessive $LaNiO_3$ and the partial coverage of active sites on CdS. Fig. 8b depicts the H_2 evolution as a function of reaction time over 30%-$LaNiO_3$/CdS nanohybrid. 737 μmol H_2 was produced over the $LaNiO_3$/CdS nanohybrid in 5 h, which was about 4.3 times that of bare CdS (172 μmol). The photocatalytic performance of 30%-$LaNiO_3$/CdS nanohybrid was also higher than that of 1.0% Pt/CdS photocatalyst (371 μmol). The results demonstrate that $LaNiO_3$ is highly active in enhancing the photocatalytic H_2 evolution of CdS-based photocatalysts. Furthermore, the H_2 evolution increased to 996 μmol in the whole Vis-NIR region. The result implied that both visible and NIR irradiation can be harvested for photocatalytic H_2 evolution over the $LaNiO_3$/CdS nanohybrid. All these results demonstrate that the introduction of $LaNiO_3$ in the $LaNiO_3$/CdS nanohybrid can promote the photocatalytic performance for H_2 evolution in the Vis-NIR region.

It is generally accepted that the combining of two semiconductors with suitable CB via the construction of a heterojunction is an effective strategy to facilitate charge transport and suppress the recombination of photoinduced electron - hole pairs in semiconductor - based photocatalysis[35-37]. Therefore, the superior photocatalytic performance observed over the $LaNiO_3$/CdS nanohybrid may be ascribed to the construction of heterojunction between $LaNiO_3$ and CdS. To confirm the existence of $LaNiO_3$/CdS heterojunction and its important role in H_2 evolution, a physical mixture of $LaNiO_3$ and CdS with a comparable $LaNiO_3$/CdS ratio (3∶7) was used for photocatalytic H_2 evolution. Compared with the $LaNiO_3$/CdS nanohybrid, the physical mixture of $LaNiO_3$ and CdS exhibited lower activity and only 198 μmol H_2 was produced in 5 h. This finding demonstrates that the heterojunction in the $LaNiO_3$/CdS nanohybrid is significant for photocatalytic H_2 evolution.

The separation and transfer efficiency of the photoinduced electrons and holes has a great effect on photocatalytic performance, so PEC tests were performed to explore the migration and separation kinetics of photoinduced electrons and holes. The room temperature photoluminescence (PL) spectra were utilized to moni-

tor the separation-recombination rate of photoinduced electrons and holes in photocatalysts to verify the charge separation effect. As shown in Fig.9a, CdS displayed a strong band edge emission at ca. 530 nm, which can be attributed to the high recombination rate of photogenerated charge carriers in CdS[38-39]. The formed $LaNiO_3$/CdS heterojunction can facilitate the transfer of the photoinduced electron-hole pairs, in accordance with the observation that the $LaNiO_3$/CdS nanohybrid displayed a PL peak with the lowest intensity. The time-resolved PL (TRPL) spectra (Fig. 9b) reveal that the fluorescence lifetime of $LaNiO_3$/CdS (4.2 ns) was much longer than that of CdS (1.0 ns), indicating that the population of surviving electrons was increased upon the combination of $LaNiO_3$, consistent with the PL quenching results. Moreover, the electrochemical impedance spectra (EIS) indicate that the $LaNiO_3$/CdS nanohybrid exhibited a smaller semicircle in the Nyquist plots compared with CdS (Fig.9c). This finding indicates that a lower charge transfer resistance in the $LaNiO_3$/CdS nanohybrid, facilitating the migration and separation of photoinduced electron-hole pairs. In addition, the transient photocurrent spectra revealed that the photocurrent of the $LaNiO_3$/CdS nanohybrid was much higher than that of CdS (Fig.9d), indicating the enhanced transfer behavior of charge carriers in the $LaNiO_3$/CdS nanohybrid. The above results demonstrate that $LaNiO_3$ could effectively promote transportation and inhibit the recombination of the photoinduced electrons and holes.

Based on the band structures of $LaNiO_3$ and CdS as well as the PEC characterizations, two possible reaction mechanisms of the photocatalytic H_2 evolution are proposed: type Ⅱ heterojunction and direct Z-scheme. The CB potential of CdS and $LaNiO_3$ was investigated by Mott-Schottky plots (Fig. S4), and the flat band potentials of CdS and $LaNiO_3$ were about −0.53 and 0.21 V (vs NHE, pH=7.0), respectively. Combined with their band-gap energies, the band structures of CdS and $LaNiO_3$ can be illustrated in Fig 10. According to conventional type Ⅱ heterojunction (Fig.10a), the photoinduced electrons on the CB of CdS can transfer to

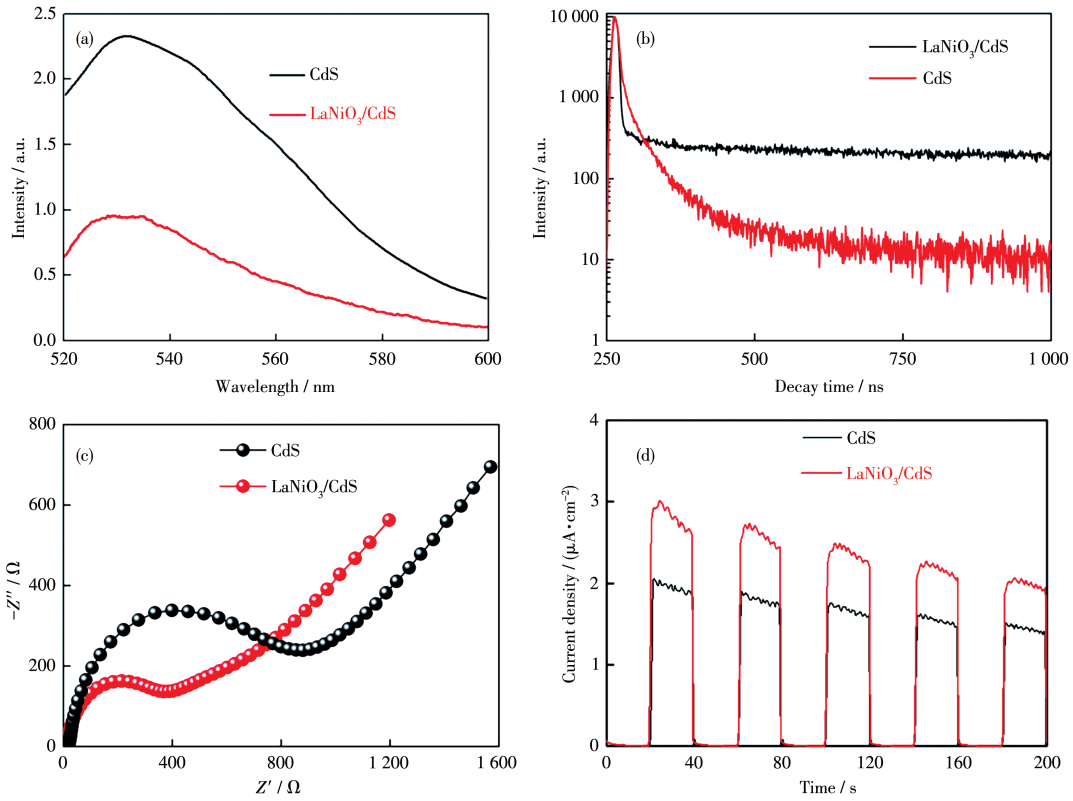

Fig.9 Steady-state PL spectra (a), TRPL spectra (b), EIS spectra (c), transient photocurrent responses (d) of CdS and the $LaNiO_3$/CdS nanohybrid

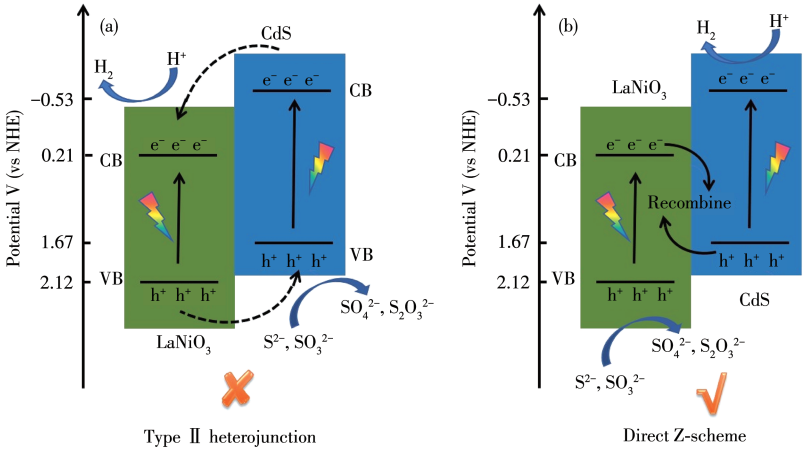

Fig.10 Proposed mechanism for H_2 evolution over direct Z-scheme $LaNiO_3$/CdS heterojunction photocatalysts

the CB of $LaNiO_3$ for H_2 evolution. However, the potential of the photogenerated electron in the CB of $LaNiO_3$ is too high for H_2 evolution, which is conflicted with the enhanced photocatalytic activity of the $LaNiO_3$/CdS nanohybrid. Therefore, the direct Z-scheme may be the most possible mechanism for photocatalytic H_2 evolution over the $LaNiO_3$/CdS nanohybrid. As shown in the direct Z-scheme $LaNiO_3$/CdS system (Fig.10b), the photoinduced electrons on the CB of $LaNiO_3$ will recombine with the photoinduced holes on the VB of CdS under visible light irradiation. In the meantime, the accumulated electrons on the CB of CdS have sufficient reduction potential for H_2 evolution, while the holes on the VB of $LaNiO_3$ can react with Na_2S-Na_2SO_3 to complete the photocatalytic redox cycle. Such a direct Z-scheme charge transfer can efficiently promote the separation of photoinduced electrons and holes, prolonging the lifetime of the electrons for boosting H_2 evolution over the $LaNiO_3$/CdS nanohybrid[40-42].

Fig. 11 shows the upconversion PL spectra of $LaNiO_3$ while excited by an 808 nm laser. The PL spectra exhibited two luminescence bands located at 406 and 628 nm, which demonstrated that $LaNiO_3$ could be excited by NIR light. As a result, the photoinduced electrons in CB of $LaNiO_3$ can recombine with the photoinduced holes in VB of CdS under Vis-NIR irradiation, facilitating the separation of the charge carrier. Moreover, the emission fluorescence at 406 nm can be absorbed by CdS in the $LaNiO_3$/CdS nanohybrid, which will contribute to photocatalytic H_2 evolution. This result was in accordance with the activity test results that the introduction of NIR could enhance the photocatalytic performance of the $LaNiO_3$/CdS nanohybrid.

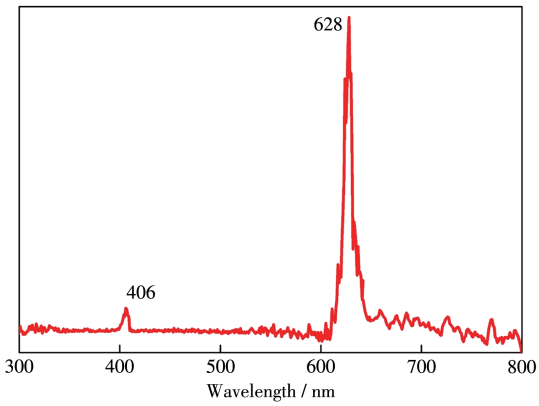

Fig.11 Upconversion PL spectra of $LaNiO_3$ while excited by an 808 nm laser

The cycling reactions were conducted to confirm direct Z-scheme charge transfer over the $LaNiO_3$/CdS nanohybrid for photocatalytic H_2 evolution, which will suppress the accumulation of photoinduced holes on CdS and consequently inhibit the photo corrosion of CdS for enhancing the photostability. As shown in Fig. 12a, the XRD pattern of the used CdS showed a new peak, ascribing to the elemental S (PDF No. 72-2402), and the CdS lost 26.7% of its original photocatalytic activity in the fourth run (Fig.13). On the contrary, the $LaNiO_3$/CdS nanohybrid exhibited enhanced stability in cycling reaction. No obvious change was observed in the XRD pattern of the used $LaNiO_3$/CdS nanohybrid and 91.9% of its original photocatalytic activity

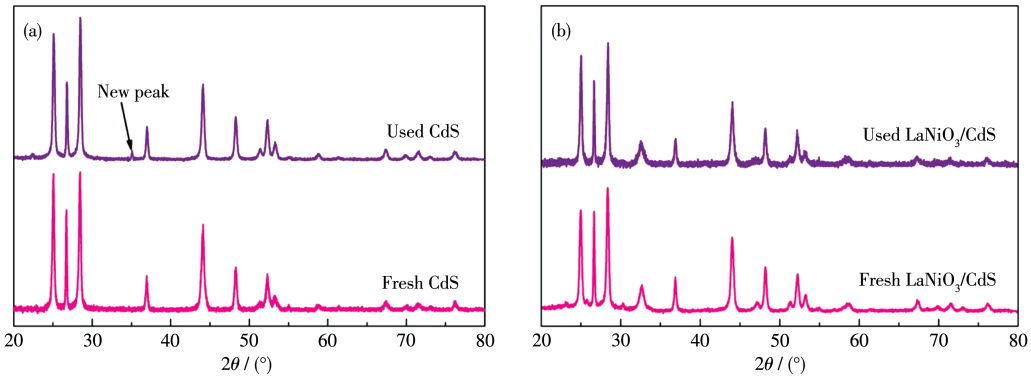

Fig.12 XRD patterns of the used and fresh CdS (a) and the $LaNiO_3$/CdS nanohybrid (b)

was maintained after four runs (Fig. 12b and Fig. 13). Based on type Ⅱ heterojunction, the photoinduced electrons and holes will accumulate in $LaNiO_3$ and CdS, respectively, and the photoinduced holes on CdS will accelerate the photo corrosion of CdS. However, the $LaNiO_3$/CdS nanohybrid exhibited enhanced stability in the cycling reaction. In addition, the detected Cd^{2+} in the filtrate from the CdS suspension was 3.2-fold that from the $LaNiO_3$/CdS nanohybrid. This result implies that photoinduced holes are transferred away from the CdS sites more effectively, inhibiting the oxidation of lattice S^{2-}. Consequently, the direct Z-scheme photocatalytic reaction mechanism can elucidate the enhanced photostability of the $LaNiO_3$/CdS nanohybrid.

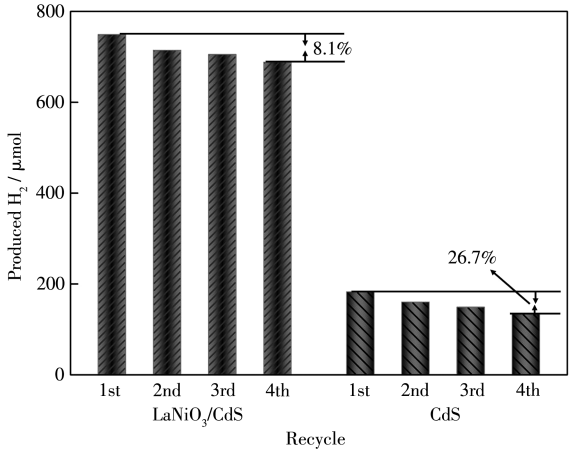

Fig.13 Cycling test of the $LaNiO_3$/CdS nanohybrid and CdS for photocatalytic H_2 evolution

3 Conclusions

In summary, the Vis-NIR light-responsive direct Z-scheme $LaNiO_3$/CdS nanohybrid was successfully synthesized and fully characterized. The as-obtained $LaNiO_3$/CdS nanohybrid showed superior photocatalytic activity for H_2 evolution due to the construction of $LaNiO_3$/CdS heterojunction as well as the enhanced light absorption in the Vis-NIR region, which was demonstrated by PEC and upconversion spectrum test. The $LaNiO_3$/CdS nanohybrid exhibited improved stability relative to CdS, which may be ascribed to the transfer away of photoinduced holes from CdS according to the direct Z-scheme heterojunction. This work provides an effective way of enhancing NIR photocatalytic H_2 evolution based on the direct Z-scheme heterojunction photocatalyst, which will be conducive to making full use of solar energy in the future.

Supporting information is available at http://www.wjhxxb.cn

References:

[1]Kudo, A, Miseki Y. Heterogeneous photocatalyst materials for water splitting. *Chem. Soc. Rev.*, **2009**,**38**:253-278

[2]Meng X G, Liu L Q, Ouyang S X, Xu H, Wang D F, Zhao, N Q, Ye J H. Nanometals for solar-to-chemical energy conversion: From semiconductor-based photocatalysis to plasmon-mediated photocatalysis and photo-thermocatalysis. *Adv. Mater.*, **2016**,**28**:6781-6803

[3]操振宇, 吴耘, 高建华. $Bi_9P_2O_{18}Cl$的相变及其可见光催化水产氢. 无机化学学报, **2022**,**38**(5):969-976
CAO Z Y, WU Y, GAO J H. $Bi_9P_2O_{18}Cl$: Phase Transition and Hydrogen Production by Photocatalytic Water-Splitting. *Chinese J. Inorg. Chem.*, **2022**,**38**(5):969-976

[4]Wang S B, Guan B Y, Lou X. Construction of $ZnIn_2S_4$-In_2O_3 hierarchical tubular heterostructures for efficient CO_2 photoreduction. *J. Am. Chem. Soc.*, **2018**,**140**:5037-5040

[5]Xu Y S, Fan M J, Yang W J, Xiao Y H, Zeng L T, Wu X, Xu Q H, Su

C L, He Q J. Homogeneous carbon/potassium-incorporation strategy for synthesizing red polymeric carbon nitride capable of near-infrared photocatalytic H_2 production. *Adv. Mater.*, **2021**,**33**:2101455

[6]Yang M Q, Gao M M, Hong M H, Ho G W. Visible-to-NIR photon harvesting: progressive engineering of catalysts for solar-powered environmental purification and fuel production. *Adv. Mater.*, **2018**, **30**: 1802894

[7]Huang W C, Gao Y, Wang J X, Ding P C, Yan M, Wu F M, Liu J, Liu D Q, Guo C S, Yang B, Cao W W. Plasmonic enhanced reactive oxygen species activation on low-work-function tungsten nitride for direct near-infrared driven photocatalysis. *Small*, **2020**,**16**:2070247

[8]Wang S B, Wang Y, Zhang A, Zang S L, Lou X. Photocatalysis: supporting ultrathin $ZnIn_2S_4$ Nanosheets on Co/N-doped graphitic carbon nanocages for efficient photocatalytic H_2 generation. *Adv. Mater.*, **2019**,**31**:1903404

[9]Wang S B, Guan B Y, Wang X, Lou X. Formation of hierarchical Co_9S_8@$ZnIn_2S_4$ heterostructured cages as an efficient photocatalyst for hydrogen evolution. *J. Am. Chem. Soc.*, **2018**,**140**:15145-15148

[10]Qi Y, Zuo Q, Mei Y Q, Yao T J, Wu J. Porous $NiCo_2O_4$ sheet catalysts for the microwave-assisted Fenton reaction. *ACS Appl. Nano Mater.*, **2020**,**3**:7152-7160

[11]Rashti A, Lu X E, Dobson A, Hassani E, Nejad F, He K, Oh T. Tuning MOF-derived Co_3O_4/$NiCo_2O_4$ nanostructures for high-performance energy storage. *ACS Appl. Energy Mater.*, **2021**,**4**:1537-1547

[12]李中钦, 陈小卫, 王艳, 程婷, 黄毅, 董鹏玉, 王勿忧, 张蓓蓓, 奚新国. $CeTiO_4$/g-C_3N_4复合材料的制备及其高效的光催化染料降解性能. *无机化学学报*, **2022**,**38**(1):53-62
LI Z Q, CHEN X W, WANG Y, CHENG T, HUANG Y, DONG P Y, WANG W Y, ZHANG B B, XI X G. Preparation of $CeTiO_4$/g-C_3N_4 composite with efficient photocatalytic activity for dye-degradation. *Chinese J. Inorg. Chem.*, **2022**,**38**(1):53-62

[13]Chen H B, Liu W X, Qin Z Z. ZnO/$ZnFe_2O_4$ nanocomposite as a broadspectrum photo-Fenton-like photocatalyst with near-infrared activity. *Catal. Sci. Technol.*, **2017**,**7**:2236-2244

[14]Wang Z Y, Peng J W, Feng X, Ding Z X, Li Z H. Wide spectrum responsive CdS/$NiTiO_3$/CoS with superior photocatalytic performance for hydrogen evolution. *Catal. Sci. Technol.*, **2017**, **7**: 2524-2530

[15]Wang Z Y, Su B, Xu J L, Hou Y D, Ding Z X. Direct Z-scheme $ZnIn_2S_4$/$LaNiO_3$ nanohybrid with enhanced photocatalytic performance for H_2 evolution. *Int. J. Hydrog. Energy*, **2020**,**45**:4113-4121

[16]Xu J L, Sun C F, Wang Z Y, Hou Y D, Ding Z X, Wang S B. Perovskite oxide $LaNiO_3$ nanoparticles for boosting H_2 evolution over commercial CdS with visible light. *Chem.-Eur. J.*, **2018**,**24**: 18512-18517

[17]Zhang G, Liu G, Wang L Z, Irvine J T S. Inorganic perovskite photocatalysts for solar energy utilization. *Chem. Soc. Rev.*, **2016**,**45**:5951-5984

[18]Lin X H, Gao Y L, Jiang M, Zhang Y F, Hou Y D, Dai W X, Wang S B, Ding, Z X. Photocatalytic CO_2 reduction promoted by uniform perovskite hydroxide $CoSn(OH)_6$ nanocubes. *Appl. Catal. B-Environ.*, **2018**,**224**:1009-1016

[19]Qin J N, Lin L H, Wang X. A perovskite oxide $LaCoO_3$ cocatalyst for efficient photocatalytic reduction of CO_2 with visible light. *Chem. Commun.*, **2018**,**54**:2272-2275

[20]Li Q, Guo B D, Yu J G, Ran J R, Zhang B H, Yan H J, Gong J R. Highly efficient visible-light-driven photocatalytic hydrogen production of CdS-cluster-decorated graphene nanosheets. *J. Am. Chem. Soc.*, **2011**,**133**:10878-10884

[21]钟秦粤, 刘瑶, 刘新梅, 张文康, 王海波. CdS@g-C_3N_4复合核壳纳米微粒的制备与光催化性能. *无机化学学报*, **2020**,**36**(5):864-874
ZHONG Q Y, LIU Y, LIU X M, ZHANG W K, WANG H B. Preparation and photocatalytic performance of CdS@g-C_3N_4 core-shell composite nanoparticles. *Chinese J. Inorg. Chem.*, **2020**,**36**(5):864-874

[22]曹丹, 安华, 严孝清, 赵宇鑫, 杨贵东, 梅辉. SiC/Pt/CdS纳米棒Z型异质结的制备及其高效光催化产氢性能. *物理化学学报*, **2020**,**36**(3):1901051
CAO D, AN H, YAN X A, ZHAO Y X, YANG G D, ME H. Fabrication of Z-scheme heterojunction of SiC/Pt/Cds nanorod for efficient photocatalytic H_2 evolution. *Acta Phys.-Chim. Sin.*, **2020**, **36**(3): 1901051

[23]Tan P F, Liu P, Zhu A Q, Zeng W X, Cui H, Pan J. Rational design of Z-scheme system based on 3D hierarchical CdS supported 0D Co_9S_8 nanoparticles for superior photocatalytic H_2 generation. *ACS Sustainable Chem. Eng.*, **2018**,**6**:10385-10394

[24]Chachvalvutikul A, Pudkon W, Luangwanta T, Thongtem T, Thongtem S, Kittiwachana S, Kaowphong S. Enhanced photocatalytic degradation of methylene blue by a direct Z-scheme Bi_2S_3/$ZnIn_2S_4$ photocatalyst. *Mater. Res. Bull.*, **2019**,**111**:53-60

[25]刘东, 陈圣韬, 李仁杰, 彭天右. 用于光催化能量转换的Z-型异质结的研究进展. *物理化学学报*, **2021**,**37**(6):2010017
LIU D, CHEN S T, LI R J, PENG T Y. Review of Z-scheme heterojunctions for photocatalytic energy conversion. *Acta Phys.-Chim. Sin.*, **2021**,**37**(6):2010017

[26]Zhang E H, Zhu Q H, Huang J H, Liu J, Tan G Q, Sun C J, Li T, Liu S, Li Y M, Wang H Z, Wan X D, Wen Z H, Fan F T, Zhang J T, Ariga K. Visually resolving the direct Z-scheme heterojunction in CdS@$ZnIn_2S_4$ hollow cubes for photocatalytic evolution of H_2 and H_2O_2 from pure water. *Appl. Catal. B-Environ.*, **2021**,**293**:120213

[27]王兆宇, 许俊丽, 张明文, 陈文韬. 直接Z型$LaNiO_3$/$Mn_{0.2}Cd_{0.8}S$异质结催化剂光解水产氢性能及机理探究. *无机化学学报*, **2021**, **37**(10):1809-1818
WANG Z Y, XU J L, ZHANG M W, CHEN W T. Direct Z-scheme $LaNiO_3$/$Mn_{0.2}Cd_{0.8}S$ heterojunction photocatalysts: enhanced photocatalytic performance for H_2 evolution and investigation of mechanism. *Chinese J. Inorg. Chem.*, **2021**,**37**(10):1809-1818

[28]Wei L, Zeng D Q, Xie Z Z, Zeng Q R, Zheng H W, Fujita T, Wei Y Z. NiO nanosheets coupled with CdS nanorods as 2D/1D heterojunction for improved photocatalytic hydrogen evolution. *Front. Chem.*, **2021**,**9**:655583

[29]Luo X, Ke Y M, Yu L, Wang Y, Homewood K, Chen X X, Gao Y. Tandem CdS/TiO_2(B) nanosheet photocatalysts for enhanced H_2 evo-

lution. *Appl. Surf. Sci.*, **2020**,**515**:145970

[30]Khettab M, Omeiri S, Sellam D, Ladjouzi M, Trari M. Characterization of $LaNiO_3$ prepared by sol-gel: Application to hydrogen evolution under visible light. *Mater. Chem. Phys.*, **2012**,**132**:625-630

[31]Zhou X S, Chen Y L, Li C F, Zhang L Q, Zhang X T, Ning X M, Zhan L, Luo J. Construction of $LaNiO_3$ nanoparticles modified g-C_3N_4 nanosheets for enhancing visible light photocatalytic activity towards tetracycline degradation. *Sep. Purif. Technol.*, **2019**,**211**:179-188

[32]Pan B, Wu Y, Qin J N, Wang C Y. Ultrathin $Co_{0.85}Se$ nanosheet co-catalyst for visible-light CO_2 photoreduction. *Catal. Today*, **2019**, **335**:208-213

[33]Jiang C K, Zhang L L, Gao F, Huang X Y, Lei R, Ye Y, Yuan J, Liu P. Promoting photocatalytic hydrogen production by a core-shell CdS@MoO_x photocatalyst connected by an S-Mo "bridge". *Catal. Sci. Technol.*, **2020**,**10**:1368-1375

[34]Liu Y, Zhang P, Tian B Z, Zhang J L. Core-shell structural CdS@SnO_2 nanorods with excellent visible light photocatalytic activity for the selective oxidation of benzyl alcohol to benzaldehyde. *ACS Appl. Mater. Interfaces*, **2015**,**7**:13849-13858

[35]Hu Y H, Schlipf J, Wussler M, Petrus M, Jaegermann W, Bein T, Buschbaum P, Docampo P. Hybrid perovskite/perovskite heterojunction solar cells. *ACS Nano*, **2016**,**10**:5999-6007

[36]Yang J S, Lin W H, Lin C Y, Wang B S, Wu J J. *n*-Fe_2O_3 to N^+-TiO_2 heterojunction photoanode for photoelectrochemical water oxidation. *ACS Appl. Mater. Interfaces*, **2015**,**7**:13314-13321

[37]Qin H, Zhao X, Zhao H K, Yan L L, Fan W L. Well-organized CN-M/CN-U/Pt-TiO_2 ternary heterojunction design for boosting photocatalytic H_2 production via electronic continuous and directional transmission. *Appl. Catal. A-Gen.*, **2019**,**576**:74-84

[38]Cheng L, Xiang Q J, Liao Y L, Zhang H W. CdS-based photocatalysts. *Energy Environ. Sci.*, **2018**,**11**:1362-1391

[39]Zhu L Y, Li H, Xia P F, Liu Z R, Xiong D H. Hierarchical ZnO decorated with CeO_2 nanoparticles as the direct Z-Scheme heterojunction for enhanced photocatalytic activity. *ACS Appl. Mater. Interfaces*, **2018**,**10**:39679-39687

[40]Fu J W, Xu Q L, Low J H, Jiang C J, Yu J G. Ultrathin 2D/2D WO_3/g-C_3N_4 step-scheme H_2-production photocatalyst. *Appl. Catal. B-Environ.*, **2019**,**243**:556-565

[41]Ye L, Wen Z H. $ZnIn_2S_4$ nanosheets decorating WO_3 nanorods core-shell hybrids for boosting visible-light photocatalysis hydrogen generation. *Int. J. Hydrog. Energy*, **2019**,**44**:3751-3759

[42]Mishra B P, Parid K. Orienting Z scheme charge transfer in graphitic carbon nitride-based systems for photocatalytic energy and environmental applications. *J. Mater. Chem. A*, **2021**,**9**:10039-10080